Potentiodynamic and electrochemical impedance spectroscopy analysis of hybrid metallic systems in 1 M HCl

Samson Dare Oguntuyi[1*], *Mandlenkosi G.R.* Mahlobo[2], *Femi J.* Akinfolarin[1], *Ngeleshi M.* Kibambe[1], *Kasongo* Nyembwe[3], *Peter M.* Mashinini[4] and *Peter* Olubambi[1]

[1]Centre for Nanoengineering and Advanced Materials (CeNAM), School of Mining, Metallurgy and Chemical Engineering, University of Johannesburg, Johannesburg, 2092, South Africa
[2]Department of Chemical and Materials Engineering, University of South Africa, P.O. Box 392, Florida 1709, South Africa
[3]Department of Mechanical and Mechatronic Engineering, Cape Peninsula University of Technology, Cape Town, South Africa.
[4]Department of Mechanical and Industrial Engineering, University of Johannesburg, Doornfontein Campus, Johannesburg 2028, South Africa

Abstract. This study evaluates the corrosion performance of hybrid aluminium components comprising built and substrate regions. The hybrid system, developed via additive and subtractive methods, was divided to separate individual parts for microstructural and electrochemical analysis in 1 M HCl using Open Circuit Potential (OCP), Electrochemical Impedance Spectroscopy (EIS), Potentiodynamic Polarization (PDP), and Chronoamperometry were used to assess corrosion kinetics, passive film stability, and time-dependent degradation. Scanning Electron Microscopy (SEM) with Energy Dispersive Spectroscopy (EDS) was used to characterize surface morphology before and after corrosion, identifying phase distribution and localized corrosion. The results pinpoint the electrochemical differences between two hybrid configurations - Sample E (Al 7 built on 6082 substrate) and Sample F (Al 10 built on 6082 substrate), with one typical configuration (Sample E) exhibiting superior corrosion resistance across both its built and substrate regions due to a more stable passive layer and refined microstructure.

1 Introduction

In environments where harsh ions like chlorides exist, corrosion remains pervasive and causes huge financial losses in the engineering systems [1]. It leads to the breakdown of metallic components, weakens structural integrity, and raises maintenance costs across a wide range of industries such as transportation, marine, aerospace, and chemical processing plants. In acidic chloride environments such as HCl, metals like aluminium are susceptible to localized corrosion processes like intergranular and pitting attack, particularly when the shielding passive films are destroyed [2, 3]. Aluminium and its alloys are hugely recognized

* Corresponding author: samsoniumdare@gmail.com

due to their ease of fabrication, outstanding strength-to-weight ratio, and intrinsic corrosion resistance, being credited to the development of a steady oxide film [4]. Although, when they are subjected to corrosive solutions, their performance can differ immensely depending on microstructure, heat treatment, alloy composition, and exposure situation. These differences become highly noticeable in hybrid systems where two or more different aluminium alloys are joined to fit intricate design and performance necessities [4, 5].

Hybrid metallic systems, sometimes called hybrid additive manufacturing (HAM), like the one fabricated by incorporating additively manufactured parts with conventional wrought or cast substrates, give design flexibility and customized performance [6]. Although, they emanate with some new corrosion challenges [7]. Hence the need to determine the corrosion performance of each part within the hybrid systems should be judiciously made. The varying processing histories and microstructures of the cast and AM-built parts could affect how each reacts to corrosive solution, making it necessary to examine their electrochemical performance distinctly to ensure the reliability and integrity of the entire structures [8].

Diverse studies have explored the corrosion performance of some hybrid systems, with a view to observing their behaviour in a corrosive environment. Parisa et al [8] reestablished damaged AA2618 alloy molds via laser powder bed fusion (L-PBF) with AlSi10Mg and examined the corrosion performance of the resulting bimetal structure in 3.5 wt.% NaCl solution. The L-PBF AlSi10Mg side demonstrated higher corrosion resistance because of its fine, homogeneous microstructure, while the cast AA2618 side exhibited poorer performance linked to detrimental intermetallic phases. Other researchers have explored the microstructural and corrosion performance of aluminium alloys [9-11], as well as the effective implementation of HAM to develop different components [5, 12, 13]. However, few or no studies have been carried out on the corrosion behaviour of a hybrid aluminium system in which two distinct aluminium alloys are individually deposited onto an identical cast aluminium alloy substrate. Hence this study addresses this gap by thoroughly examining the corrosion activity of the two typical distinct regions, such as the selective laser melted (SLM-built) region and the cast substrate region, thus providing new understandings into the electrochemical behaviour differences with such hybrid structures. The examination was carried out in a 1 M HCl solution applying a combination of OCP, PDP, chronoamperometry, and EIS. These techniques give insights into the system's passive film behaviour, corrosion kinetics, and susceptibility to disintegration. Also, microstructural assessments via SEM with EDS were carried out to relate electrochemical performance to their composition and surface morphology. By combining the microstructural and electrochemical analyses, this study aims to establish an understanding of the reliability and durability of hybrid aluminium structures in aggressive acidic solutions. This knowledge is essential for aerospace, automotive industries, as well as industrial marine applications that require hybrid aluminium components combining the unique properties of specific alloys with a common cast substrate. Such components must survive aggressive acidic environments, thus sustaining their structural integrity, reducing production costs, and contributing to innovation in materials design and corrosion control for structural applications.

2 Methodology

2.1 Sample preparation

The hybrid metallic samples (consisting of the built and substrate) used in this study were fabricated by depositing two distinct additively manufactured (AM) aluminium alloys, referred to hereafter as Al 7 and Al 10, which refer to alloys with 7 wt% and 10 wt% of Si, onto a base substrate made from cast aluminium 6082. The selective laser manufacturing

(SLM) process used gas-atomized Al–Si powders and a stripe scanning strategy to maintain even heat distribution and a homogeneous microstructure to create the build on the substrate. Processing parameters, including 370 W laser power, 1200 mm/s scan speed, 0.11 mm hatch spacing, and 30 µm layer thickness, were judiciously chosen, with a 67° layer rotation applied to minimize anisotropy and residual stresses. The substrate region was fabricated from Al 6082 alloy using conventional gravity casting, with the molten alloy (≈ 700–750 °C) poured into a sand mold and left to cool at room temperature. Their compositions are presented in Table 1, with corresponding labels shown in Figure 1. To ensure focused examination, the hybrid system was judiciously sectioned (as depicted in Figure 1) to separate each region of interest, allowing distinct assessment of Al 7, Al 10, and the 6082 substrate areas.

The samples were mounted in epoxy resin, and their opened surfaces were carefully prepared through a step-by-step grinding process using silicon carbide (SiC) abrasive papers of progressively finer grit sizes. Then followed by polishing with a diamond suspension down to a 1 µm finish, producing a smooth, mirror-like surface appropriate for electrochemical testing and microscopic examination.

Table 1. Compositions of hybrid components (built and substrate materials).

Alloys	Elements							
	Fe	Ti	Cu	Zn	Si	Cr	Mg	Al
Al 7 (wt.%)	0.10	0.15	0.25	0.50	7.0	0.10	0.40	Remaining
Al 10 (wt.%)	0.10	0.15	0.25	0.50	10.0	0.40	0.10	Remaining
Al 6082 (wt.%)	0.35	0.15	0.30	0.15	0.8	0.30	1.00	Remaining

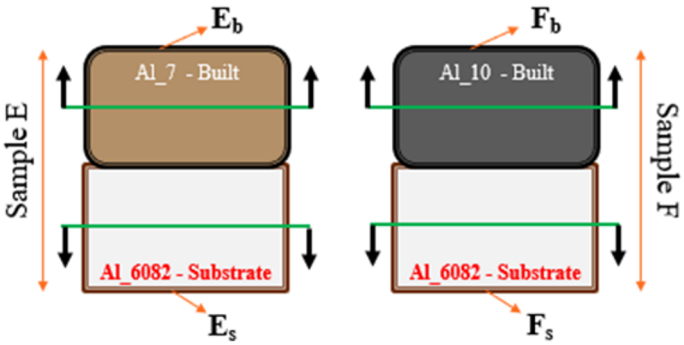

Fig. 1. Description of the hybrid samples, their labelling, and sectioning method.

2.2 Electrochemical testing

Electrochemical testing was performed using a standard three-electrode setup connected to Gamry Reference 600+ potentiostat. The sample served as the working electrode, with a saturated calomel electrode (SCE) acting as the reference and a platinum mesh as the counter electrode. A 1 M HCl solution was used as the electrolyte throughout the experiments, freshly prepared with analytical-grade reagents and deionized water. The corrosion performance of the samples was investigated using a run of electrochemical techniques, each providing insights into various features of their performance. To ensure reproducibility, all experiments were performed three times; only representative curves are shown here for simplicity.

- OCP: Before testing began, individual samples were immersed in the test solution and left uninterrupted for 7200 seconds. During this time, the OCP was continuously monitored to allow the system to reach a stable, steady-state potential.
- PDP: In assessing the corrosion potential and current density, a linear sweep voltammetry test was carried out. The scan started at 250 mV below and ended at 250 mV above the OCP, progressing at a scan rate of 0.01 V/s.
- EIS: EIS measurements were taken at the stabilized OCP using a small AC voltage of 10 mV. The frequency ranged from 100 kHz down to 10 mHz, helping to reveal details about charge transfer resistance and the capacitive nature of the system.
- Chronoamperometry: Finally, to evaluate long-term stability and detect tendencies for localized corrosion, a constant potential (E_{corr}) was applied for 3600s, while recording the current over time.

2.3 Microstructural analysis

Before and after the electrochemical tests, selected samples were examined using SEM along with EDS. This allowed for a closer look at the surface features and microstructural details, such as grain orientation and any signs of intergranular corrosion or localized damage.

3 Results and discussion

3.1 Open circuit potential

Over an extended immersion period of 2 hr in a 1 M HCl solution, the OCP behaviour of the hybrid structures was evaluated. Figure 2 shows the potential variation as a function of time for four samples sectioned from the hybrid configurations, designated as E_b, E_s, F_b, and F_s, corresponding to the built and substrate regions of samples E and F, respectively. Each plot depicts the corrosion tendencies and thermodynamic consistency of the respective regions of the samples.

Within the early seconds of immersion, the Sample F_b reveals a sharp rise in potential, stabilizing near -0.80 V, demonstrating quick surface stabilization or development of passive film. Meanwhile, F_s commence at a more noble potential of about -0.78 V and linger to change progressively to more positive values, getting beyond -0.74 V after about 7000 seconds. This constant rising indicates the existence of a higher corrosion-resistant layer, which can be a result of passive film improvement, refined microstructure, or compositional variations in the substrate part of sample F [9]. Sample E_s and E_b collectively commence at potentials near -0.84 V, which are more negative in contrast to sample F. This indicates that sample E is more susceptible to corrosion. E_s experiences a minute change toward nobler potential, approaching about -0.83 V, while E_b reveals a gradual lift over time, stabilizing a little below -0.84 V. The less change and persistent negative potentials for sample E indicate less development of stable surface film, restricted passivation, or mixed surface activity, which can be attributed to microstructural inconsistencies in the built and substrate areas [8, 10].

Contrasting the two hybrid systems, sample E and sample F, as well as their examined sections. F_s depicts the most noble OCP, signifying the optimum corrosion resistance, this can be credited to the beneficial microstructural properties in the sections [8]. F_b similarly demonstrates appreciable consistency, with only a little change from F_s, which may signify coherence between the substrate and built regions in sample F. On the other hand, sample E indicates lesser corrosion resistance, with either of the built and substrate sections stabilizing at higher negative potentials. This outcome can be ascribed to inherent variations in

metallurgical features, like residual stresses, grain boundary density, phase distributions, and the thermal disparity of the two sections affected by the fusion zone of the laser, consequently influencing stability and film development [14, 15].

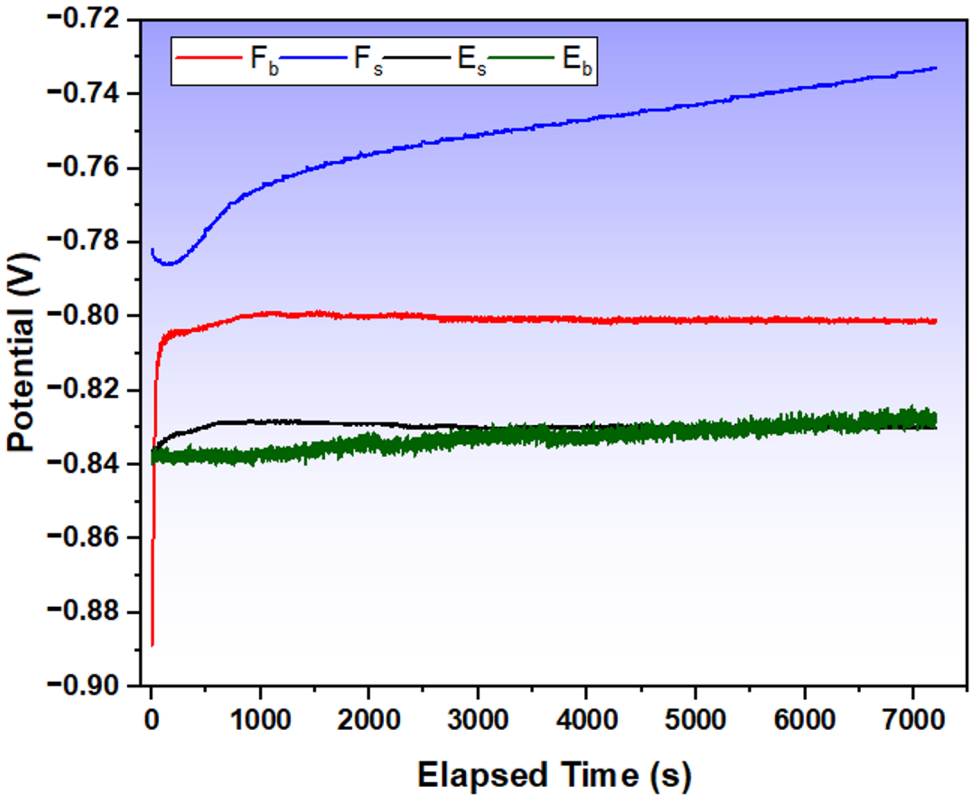

Fig. 2. OCP measurement for the hybrid structured samples (E_b, E_s, F_b, and F_s) immersed in 1 M HCl solution.

3.2 Potentiodynamic polarization

This section states the electrochemical response of the two hybrid aluminium samples, with each sample divided into its built and substrate sections for corrosion comparison. Using PDP, the corrosion performance of the four regions, E_b, E_s, F_b, and F_s, was examined. Figure 3 depicts the outcome of the polarization plots, which gives an explicit insight into the corrosion mechanisms at work at each zone. Some key parameters, like the corrosion potential (E_{corr}), corrosion current density (I_{corr}), and Tafel slopes (B_a and B_c), were extracted via Tafel extrapolation and are stated in Table 2.

F_b demonstrated the highest corrosion resistance among the examined regions, characterized by a comparatively noble corrosion potential (E_{corr}) of −717.648 mV vs. SCE, and a low corrosion current density (I_{corr}) of 158.887 mA/cm². Though Fs had a slightly more negative E_{corr} (−783.7 mV), it recorded the lowest I_{corr} (100.178 mA/cm²), indicating a more stable passive layer and a decline in corrosion susceptibility in that region. In comparison, the built and the substrate region, E_b and E_s, depicted a more negative Ecorr data (−792.690 mV and −812.964 mV, respectively), together with higher I_{corr} values, 243.307 mA/cm² for E_b and 200.980 mA/cm² for E_s, thus demonstrating higher susceptibility and less efficient passivation [15].

Therefore, regarding overall corrosion performance, the order based on combined E_{corr} and I_{corr} results can be ranked in descending order as: $F_s > F_b > E_s > E_b$. This sequence suggests that the F-based hybrid regions are ascribed to benefit from superior microstructural features, like refined grain structures or denser, more protective oxide films, which contribute to their improved corrosion performance [12].

Further observation of the polarization curves reveals unique variations in the anodic and cathodic behaviour. Examining the anodic parts of the samples, Fs depicted a relatively flat anodic slope, signifying the existence of a stable passive layer, thus ensuring a slower metal dissolution rate. On the other hand, E_b depicted a sharp anodic increase, indicative of rapid anodic dissolution and inadequate passivation behaviour. The regions of the hybrid structure labelled F_b and E_s demonstrated intermediate trends, implying limited or unstable passivation under the test conditions. Also, both E_s and F_s curves showed signs of anodic instability, characterized by sudden fluctuations in current density. These fluctuations are referred to as metastable pitting, in which brief localized passive layer breakdown occurs, accompanied by quick repassivation. The Es among the two experienced more current oscillations, pinpointing a greater susceptibility to localized corrosion occurrence in that section [16].

All samples displayed hydrogen evolution, a feature exemplified at the cathodic segment, which is a common phenomenon in acidic corrosion environments. Once again, among the examined hybrid region, Fs showed the least cathodic current density, reinforcing its overall superior corrosion resistance [8]. Juxtaposing the SLM-built samples based on their Silicon contents, the sample with higher silicon (10 wt% Si) composition - F_b promotes the establishment of better stabilized and protective oxide film, thus improving its corrosion resistance. The oxide layer performs as a huge shield against a harsh acidic environment, consequently minimizing metal dissolution [12]. Conversely, sample E_b (7 wt% Si), with its lesser silicon concentration, develops a low robust passive layer, making it more prone to acidic attack, corresponding to the higher current density [11, 15].

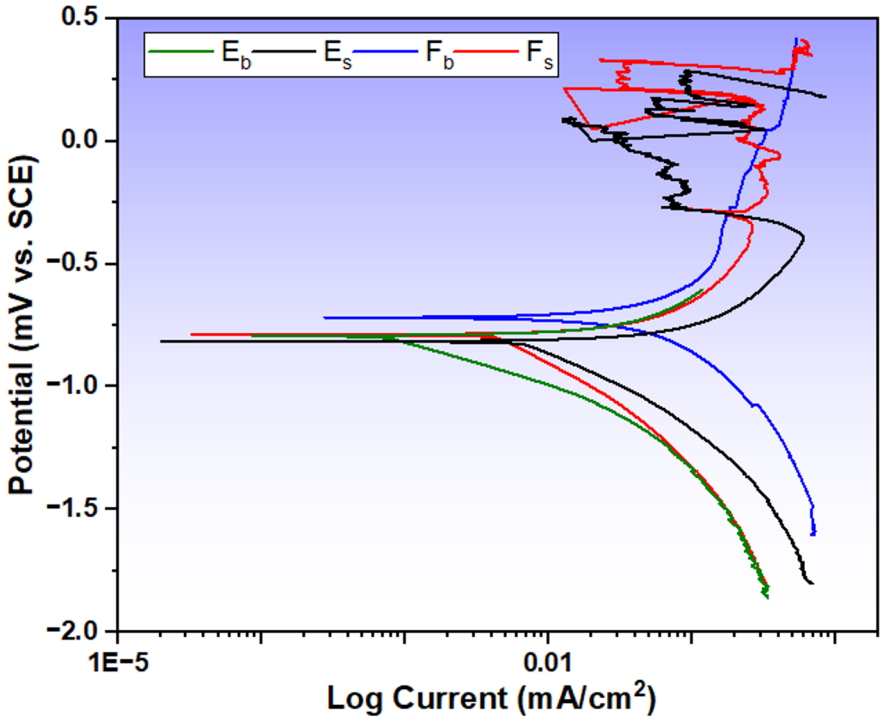

Fig. 3. PDP curves of hybrid structured samples (E_b, E_s, F_b, and F_s) immersed in 1 M HCl solution.

Table 2. Summarizes the estimated corrosion parameters obtained via Tafel extrapolation from the polarization curves

Sample	E_{corr} (mV vs. SCE)	I_{corr} (mA/cm²)	B_c	B_a
F_b	-717.648	158.887	591.249	591.249
F_s	-783.656	100.178	582.830	937.938
E_b	-792.69	243.307	395.077	441.692
E_s	-812.964	200.980	439.055	439.055

3.3 Chronoamperometry analysis

Figure 4 depicts the chronoamperometric performance of the four samples E_b, E_s, F_b, and F_s across a 1-hour immersion duration in a 1 M HCl solution. The current density (A/cm²) is plotted against time to explore how surface passivation and electrochemical performance of the different alloy samples emerge over time.

At the commencement of the test (around 0 seconds), all the samples depict a transient current reaction, which reflects the initial relationship between the electrolyte and the sample surfaces, including double-layer charging influences [17]. E_b sample reflects a sharp spike in anodic current, going beyond 0.015 A/cm². This high current response indicates an extremely reactive surface experiencing rapid anodic dissolution, reflecting poor initial passivation and a susceptibility to protective films breakdown or localized corrosion [15]. The sample, F_b, also reflects a quick increment in current; however, it remains consistent around 0.0055 A/cm². This performance indicates a short activation phase followed by sharp development of a shielding passive layer, demonstrating good initial corrosion resistance [16]. The F_b sample commences with a moderate current that progressively decreases to a lesser value than E_s, depicting slower, although more efficient passivation and better stability in corrosion resistance. The sample F_s shows a unique behaviour, commencing with a negative current (approximately -0.006 A/cm²). This indicates that cathodic reactions, like hydrogen evolution or oxygen reduction, are more prominent on its surface. The fact that the negative current remains stable throughout the test reflects strong electrochemical stability and a surface that has less corrosion vulnerability [17].

Therefore, the corrosion protection behaviour follows the hierarchy $F_s > F_b > E_s > E_b$. Confirming that F_s demonstrates excellent stability and strong cathodic performance throughout the test. This signifies less corrosion occurrence, establishing it as the most corrosion-resistant among the samples. F_b depicts quick initial passivation followed by a steady anodic current. While not as resistant as F_s, it still gives adequate protection against corrosion. The sample F_b takes a long time to stabilize, but finally develops a more efficient passive layer than E_s. It offers moderate corrosion resistance. The E_b sample exhibits a high and constant anodic current, demonstrating the highest reactive surface with poor passivation. Moreover, at around 400 s there was a drop in the anodic current for E_b, which continued till about 3200 s where its current drop below Es, this performance is ascribed to the initiation of its high current at the commencement and instability in the formation of stable films over time, in contrast sample E_s, showed a more stable film formation. In spite of this crossover, these factors contribute to categorizing sample E_b as the least corrosion resistant [19].

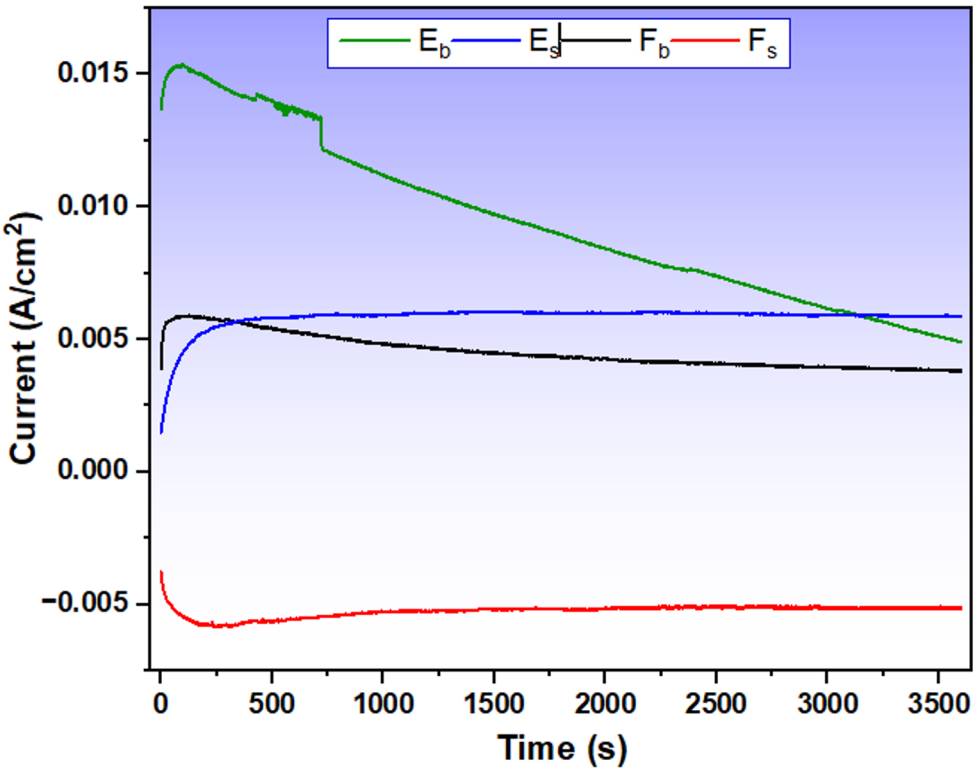

Fig. 4. Chronoamperometric response showing current density over time for hybrid samples E_b, E_s, F_b, and F_s, highlighting differences in electrochemical stability and corrosion behavior.

3.4 Electrochemical impedance spectroscopy

The Nyquist plot shown in Figure 5 illustrates significant variations in the electrochemical impedance behavior of the hybrid samples, with corrosion performance assessed by plotting the imaginary component (Zim) against the real component (Zre). Among the four regions examined. F_s reveals the most prominent semicircular arc on the Nyquist graph, featured by the optimum values on both the Zre and Zim axes. This performance signifies excellent corrosion resistance and pinpoints the development of a consistent, shielding layer [18]. The elevated impedance values are reflections of slower charge transfer kinetics and improved electrochemical stability, referencing F_s as the most corrosion-resistant section of the hybrid system of sample F. While F_b, which represents the built region of Sample F, shows comparatively high impedance results, but not as high as the one observed in F_s. The moderately sized arc reveals effective passivation and a good degree of corrosion. The slightly lesser behaviour in contrast to F_s may be ascribed to differences in microstructure or surface uniformity, as depicted in Figure 6, being introduced during the AM process [17].

In comparison, Es, depicting the substrate region of sample E, exhibited a higher horizontally stretched impedance arc along the Zre axis. This reflects an increase in resistive performance, which is ascribed to surface irregularities or heterogeneous corrosion behavior. Although, E_s shows some level of corrosion resistance, its shielding performance looks erratic, indicating localized deterioration or imperfections in the passive film. While the E_b section, signifying the build of the hybrid sample E, shows on the plot the least impedance values with a compressed and shallow arc. This indicates poor corrosion resistance and spontaneous charge transfer, which can be directly influenced by an unstable or thin passive

film. Hence, the E_b region appears to be the most vulnerable to corrosion among all the regions examined [18].

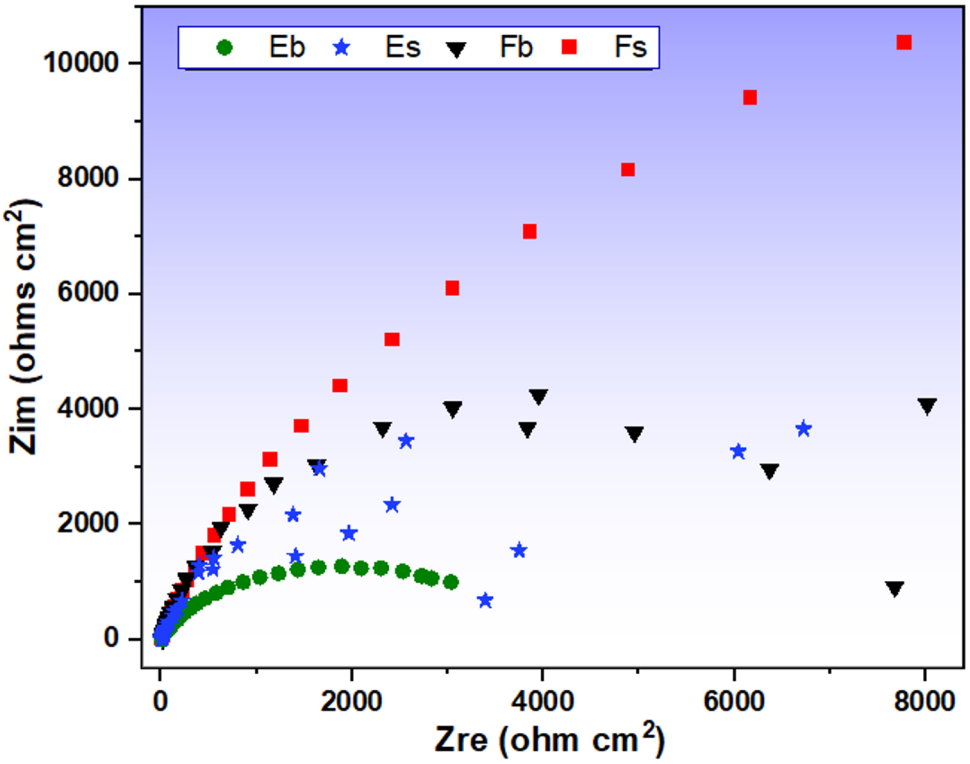

Fig. 5. Nyquist plot showing the electrochemical impedance response of hybrid samples (E_b, E_s, F_b, and F_s) with distinct variations in corrosion resistance based on real (Z′) and imaginary (Z″) impedance components.

3.5 Microstructural analysis

Figure 6 shows the microstructures of the examined samples (E_b, E_s, F_b, and F_s) captured via SEM to reveal the microstructural features and surface morphology before corrosion. Distinct differences were observed in porosity distribution, grain structure, and surface integrity. Samples F_s and F_b exhibited relatively fewer pores, dense structures, and smooth surfaces with fine grains, likely reflecting well-optimized processing techniques. Also, uniform grain distribution and minimal defects were noted, indicating excellent surface homogeneity and quality [19]. In contrast, samples E_b and E_s displayed coarser grain structures with evident microvoids, pores, and irregularities, suggesting a less refined microstructure and an increased likelihood of corrosion initiation. Furthermore, the built regions (F_b and E_b) exhibited signs of anisotropy associated with the manufacturing process, which could influence their corrosion behaviour [20].

Figure 7 presents SEM evaluations of the samples after corrosion. Significant variation in surface deterioration was observed among the samples. E_b exhibited the most extensive damage, including delamination, deep pitting, and oxide formation, indicating poor corrosion resistance. E_s showed localized corrosion but was relatively less affected, suggesting improved passivation behaviour. F_b underwent moderate corrosion with some pitting and oxide coverage, while F_s showed the least degradation, maintaining a largely intact surface

with only minor oxide formation, highlighting its highest corrosion resistance. EDS analysis (Figure 8) performed after corrosion further confirmed differences in surface chemistry, especially oxide development and elemental distribution around the entire corroded regions. The weight percentages of oxygen and chlorine detected by EDS indicate the formation of corrosion products, such as aluminum oxides, chlorides, and other compounds. As depicted in the SEM image (Fig. 7), these findings correspond to different stages of localized corrosion progression, including pitting initiation, crack propagation, surface degradation, and delamination of the hybrid-manufactured Al-Si-Mg samples after exposure to the 1 M HCl solution [15].

The higher silicon proportion in sample F_b (10 wt% Si) compared to E_b (7 wt% Si) has an important effect in refining its microstructure. Consequently, elevating the volume fraction of silicon phases does not exclusively aid in grain size refinement but equally influences the formation of intermetallic compounds within the alloy [5, 13]. These resulting microstructural characteristics impact how the alloys perform mechanically and electrochemically, which helps elucidate the variation in performance of F_b and E_b despite having a similar processing route [9, 18].

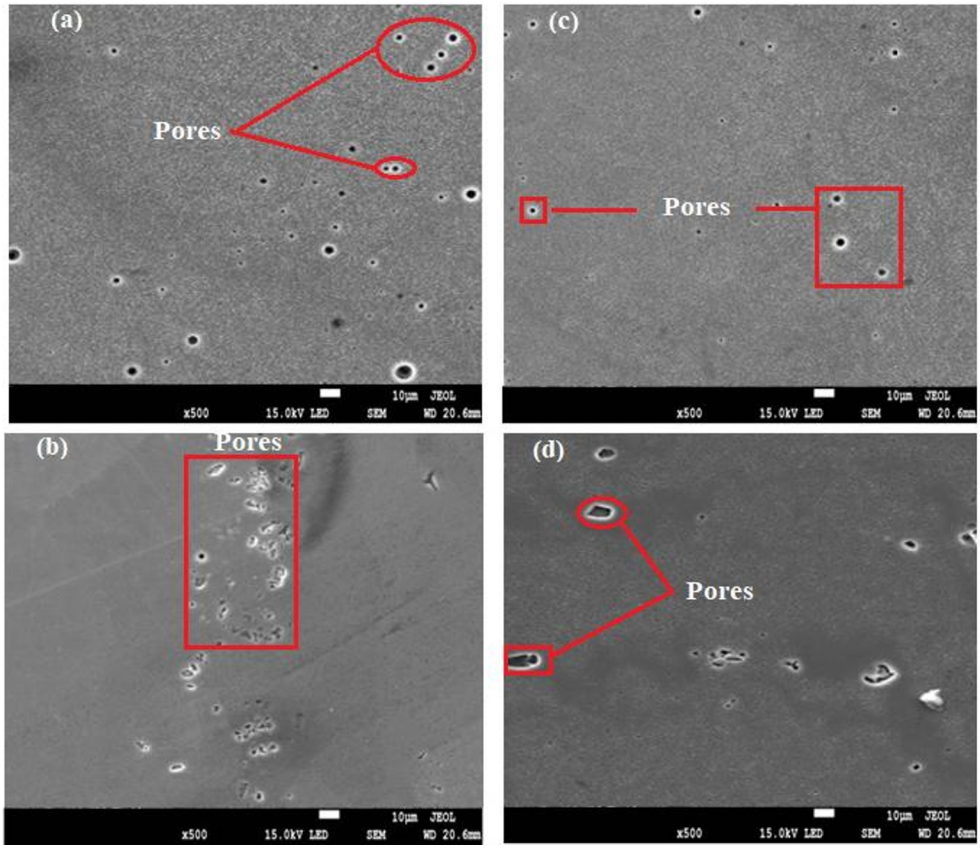

Fig. 6. SEM images of the built and substrate section of the hybrid configurations prior to corrosion: (a) E_b, (b) E_s, (c) F_b, and (d) F_s.

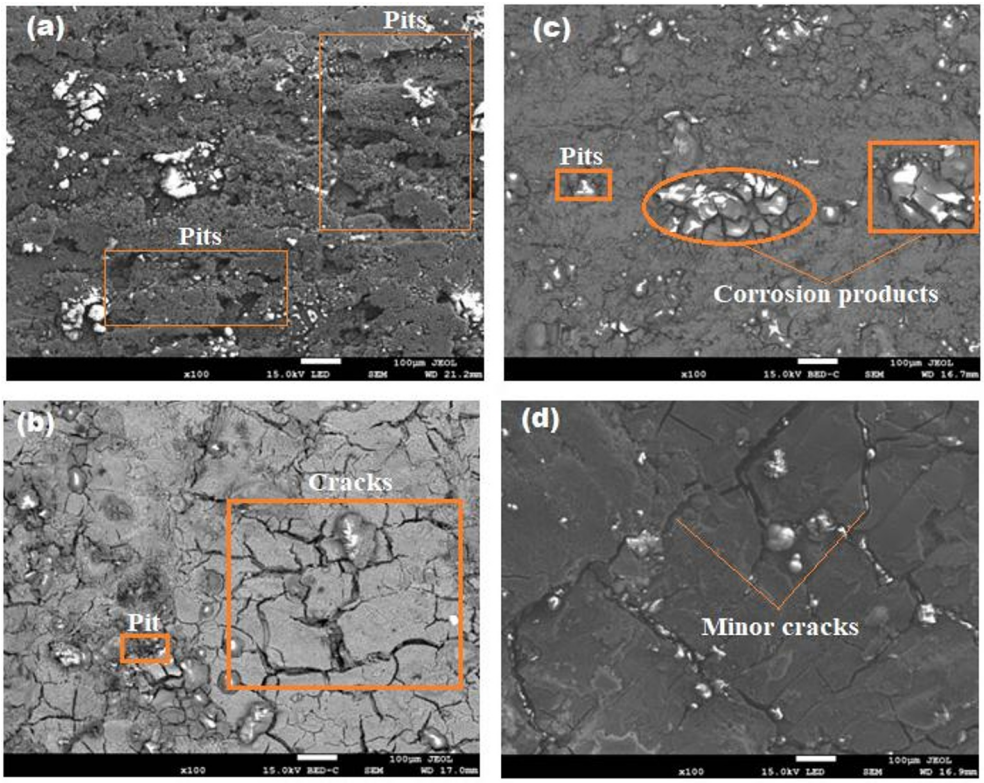

Fig. 7. SEM images of the built and substrate section of the hybrid configurations after corrosion: (a) E_b, (b) E_s, (c) F_b, and (d) F_s.

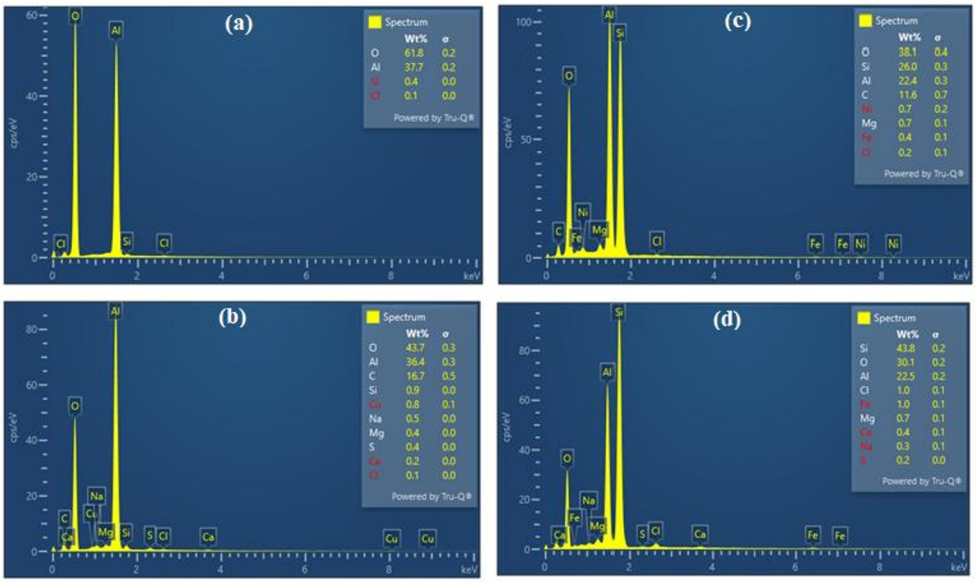

Fig. 8. EDS analysis of each entire corroded sample after corrosion exposure, showing elemental distribution and corrosion product formation: (a) E_b, (b) E_s, (c) F_b, and (d) F_s.

Conclusion

This work conducted a thorough examination via OCP, PDP, chronoamperometry, EIS, and SEM with EDS to evaluate the corrosion performance of HAM Al alloys. The results highlight the electrochemical differences between the distinct regions of two hybrid configurations, with one configuration exhibiting superior corrosion resistance across both its built and substrate regions due to a more stable passive layer and refined microstructure. The enhanced performance can be attributed to the increased silicon concentration, specifically in the SLM-built region F_b, which contains 10 wt% Si, compared to the other hybrid sample's SLM-built region E_b, which contains 7 wt% Si. Surface analysis of the latter revealed microstructural defects, porosity, and oxide formation in the built sections, contributing to delamination, pitting, and localized corrosion, making it the least corrosion-resistant among all examined regions of the hybrid structures. Furthermore, the cast substrates exhibited contrasting corrosion performances despite being made from similar alloys and processed via similar routes, which pinpoints the impact of microstructural factors beyond composition alone. Overall, these findings emphasize that refining microstructure, most importantly through silicon composition and controlling defects during the additive manufacturing process, is important for improving the corrosion resistance and long-term durability of hybrid additive-manufactured aluminium components.

The authors gratefully acknowledge the University of Johannesburg, South Africa, for its support. This research was conducted with the assistance of the Centre for Nanoengineering and Advanced Materials, University of Johannesburg.
Data availability: Data supporting the findings of this study are available from the corresponding authors upon reasonable request

References

1. S.S. Rajahram, T.J. Harvey, R.J.K. Wood, Erosion–corrosion resistance of engineering materials in various test conditions. Wear 267, 244 (2009). https://doi.org/10.1016/j.wear.2009.01.052
2. A.K. Mishra, N. Ebrahimi, D.W. Shoesmith, P.E. Manning, Materials selection for use in concentrated hydrochloric acid. NACE (2016), NACE-2016. https://doi.org/10.5006/2193
3. R. Fan, W. Zhang, Y. Wang, D. Chen, Y. Zhang, Metal material resistant to hydrochloric acid corrosion. IOP Conf. Ser. Mater. Sci. Eng. **1732**, 012134 (2021).
4. M.A. Wahid, A.N. Siddiquee, Z.A. Khan, Aluminum alloys in marine construction: characteristics, application, and problems from a fabrication viewpoint. Mar. Syst. Ocean Technol. **15**, 70 (2020). https://doi.org/10.1007/s40868-019-00069-w
5. S. Shakerin, A. Hadadzadeh, B.S. Amirkhiz, S. Shamsdini, J. Li, M. Mohammadi, Additive manufacturing of maraging steel-H13 bimetals using laser powder bed fusion technique. Addit. Manuf. **29**, 100797 (2019). https://doi.org/10.1016/j.addma.2019.100797
6. K. Nyamuchiwa, R. Palad, J. Panlican, Y. Tian, C. Aranas Jr, Recent progress in hybrid additive manufacturing of metallic materials. Appl. Sci. **13**, 8383 (2023). https://doi.org/10.3390/app13148383
7. M.E. Korkmaz, S. Waqar, A. Garcia-Collado, M.K. Gupta, G.M. Krolczyk, A technical overview of metallic parts in hybrid additive manufacturing industry. J. Mater. Res. Technol. **18**, 384 (2022). https://doi.org/10.1016/j.jmrt.2022.02.085
8. I.H. ZainElabdeen, L. Ismail, O.F. Mohamed, K.A. Khan, A. Schiffer, Recent advancements in hybrid additive manufacturing of similar and dissimilar metals via

laser powder bed fusion. Mater. Sci. Eng. A, 146833 (2024). https://doi.org/10.1016/j.msea.2024.146833
9. D.R. Ramya, R.D. Pruthviraj, Potentiodynamic Studies of Aluminium 2024 Alloy in Different Concentration of Hydrochloric Acid Medium at Laboratory Temperature. J. Mater. Sci. **10**, 2321 (2017).
10. F.V. Adams, S.O. Akinwamide, B. Obadele, P.A. Olubambi, Comparison study on the corrosion behavior of aluminum alloys in different acidic media. Mater. Today: Proc. **38**, 1040 (2021). https://doi.org/10.1016/j.matpr.2020.05.781
11. S.A. Raza, M.R.A. Karim, T. Shehbaz, A.A. Taimoor, R. Ali, M.I. Khan, Effect of pH and concentration on electrochemical corrosion behavior of aluminum Al-7075 T6 alloy in NaCl aqueous environment. J. Electrochem. Sci. Technol. **13**, 213 (2022). https://doi.org/10.33961/jecst.2020.01214
12. L. Kučerová, I. Zetková, Š. Jeníček, K. Burdová, Hybrid parts produced by deposition of 18Ni300 maraging steel via selective laser melting on forged and heat treated advanced high strength steel. Addit. Manuf. **32**, 101108 (2020). https://doi.org/10.1016/j.addma.2020.101108
13. Y. Uematsu, T. Kakiuchi, M. Nakajima, K. Matsuo, Microstructures and fatigue behavior of additively manufactured maraging steel deposited on conventionally manufactured base plate. J. Mater. Eng. Perform. **30**, 4902 (2021). https://doi.org/10.1007/s11665-021-05548-z
14. Y. Tan, Sens. Sensing localised corrosion by means of electrochemical noise detection and analysis. Actuators B Chem. **139**, 688 (2009). https://doi.org/10.1016/j.snb.2009.03.061
15. F. Andreatta, H. Terryn, J.H.W. De Wit, Corrosion behaviour of different tempers of AA7075 aluminium alloy. Electrochim. Acta **49**, 2851 (2004). https://doi.org/10.1016/j.electacta.2004.01.046
16. C. Wang et al., Effects of rare earth modifying inclusions on the pitting corrosion of 13Cr4Ni martensitic stainless steel. J. Mater. Sci. Technol. **93**, 232 (2021). https://doi.org/10.1016/j.jmst.2021.03.014
17. M.C. Li, Y.F. Cheng, Corrosion of the stressed pipe steel in carbonate–bicarbonate solution studied by scanning localized electrochemical impedance spectroscopy. Electrochim. Acta **53**, 2831 (2008). https://doi.org/10.1016/j.electacta.2007.10.077
18. H.H. Hernández, A.M.R. Reynoso, C. Juan, T. González, C.O.G. Morán, Electrochemical Impedance Spectroscopy (EIS): A Review Study of Basic Aspects of the Corrosion Mechanism Applied to Electrochem. Impedance Spectrosc., 1 (2020).
19. P. Forcellese, T. Mancia, M. Simoncini, T. Bellezze, Characterization of Microstructure and Localized Corrosion Resistance of Heat-Treated 17-4 PH Stainless Steel Fabricated by Material Extrusion. Metals **15**, 137 (2025). https://doi.org/10.3390/met15020137
20. S. Sahu, Pitting Corrosion Behavior of Multi Principal Element Alloys, Doctoral dissertation, The Ohio State University, (2022).